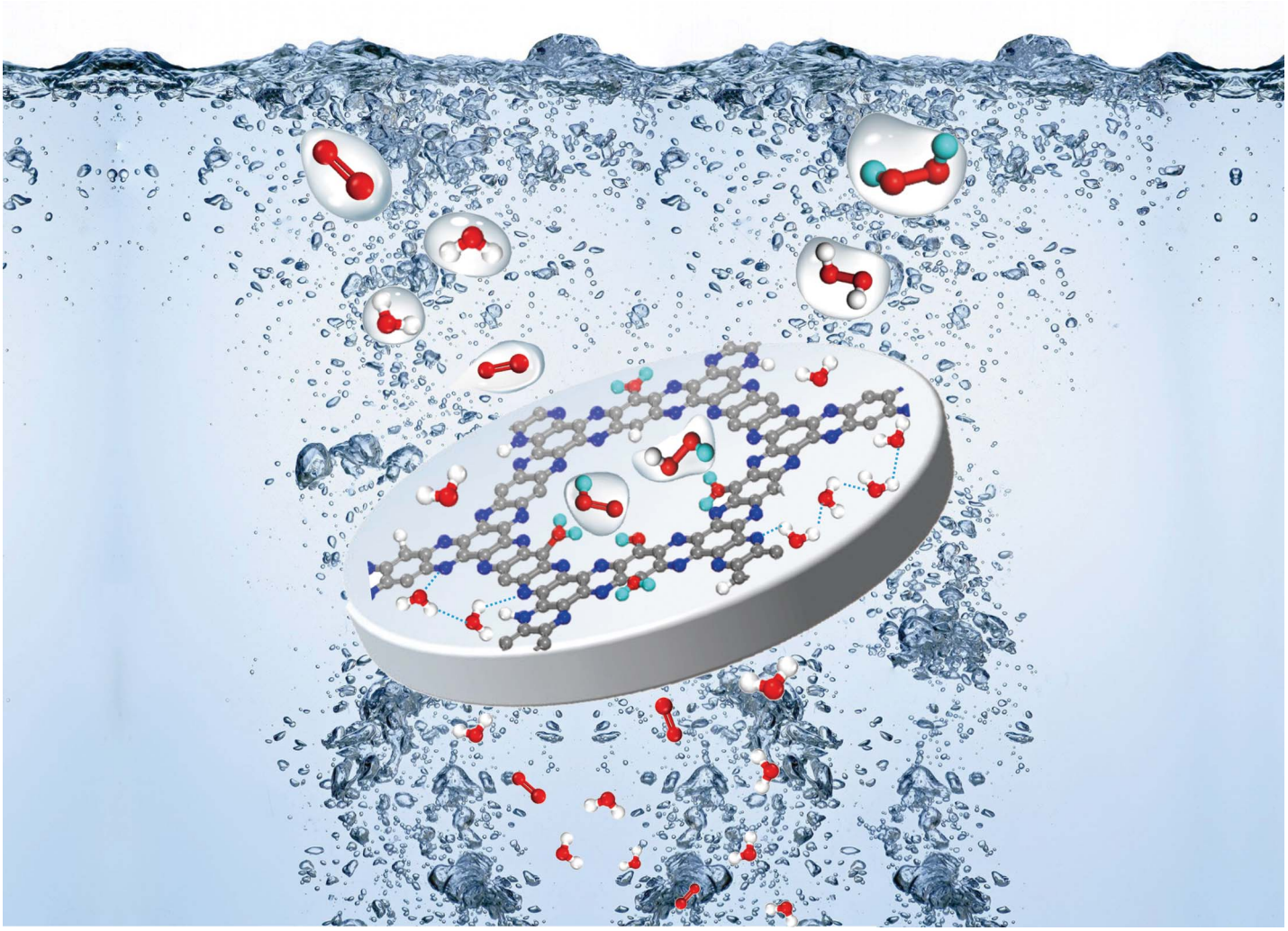

Showcasing a fundamental study of liquid water interacting with gaseous oxygen on g-C_5N_2 catalysts to produce hydrogen peroxide by a group of researchers led by Prof. Liangliang Huang from the University of Oklahoma and Prof. Jianguo Wang from Zhejiang University of Technology. Hydrogen Peroxide Synthesis on Porous Graphitic Carbon Nitride Using Water as Hydrogen Source.

Hydrogen peroxide synthesis on porous graphitic carbon nitride using water as a hydrogen source

Using water as a hydrogen source is a promising strategy for alternative hydrogen peroxide synthesis. By using g-C_5N_2 as the catalyst, the liquid water/gaseous oxygen reaction to produce hydrogen peroxide has been computationally investigated. The two-step reaction mechanism depends on: (a) water adsorption and activation at unsaturated carbon sites of g-C_5N_2; (b) the formation of a proton transfer cluster, consisting of both interfacial hydrogen bonded water and adsorbed water at g-C_5N_2.

As featured in:

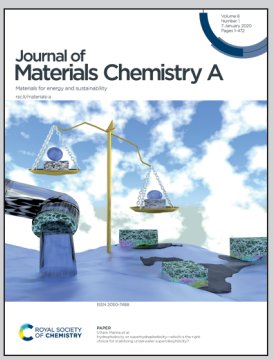

See Liangliang Huang, Jianguo Wang *et al.*, *J. Mater. Chem. A*, 2020, **8**, 124.

ROYAL SOCIETY OF CHEMISTRY

rsc.li/materials-a

Registered charity number: 207890

Journal of Materials Chemistry A

PAPER

View Article Online
View Journal | View Issue

Cite this: J. Mater. Chem. A, 2020, 8, 124

Hydrogen peroxide synthesis on porous graphitic carbon nitride using water as a hydrogen source†

Yongyong Cao,[a] Guobing Zhou,[b] Xianlang Chen,[a] Qi Qiao,[b] Chenxia Zhao,[a] Xiang Sun,[a] Xing Zhong,[a] Guilin Zhuang,[a] Shengwei Deng,[a] Zhongzhe Wei,[a] Zihao Yao,[a] Liangliang Huang *[b] and Jianguo Wang *[a]

Received 26th July 2019
Accepted 24th October 2019

DOI: 10.1039/c9ta08103h

rsc.li/materials-a

Using water as a hydrogen source is a promising strategy for alternative hydrogen peroxide (H_2O_2) synthesis. By a series of *ab initio* molecular dynamics (AIMD) simulations and reactive molecular dynamics (RxMD) calculations, fundamental details have been revealed regarding how liquid water interacts with oxygen on a metal-free carbon nitride catalyst, and the two-step reaction mechanism of H_2O_2 synthesis. Metal-free porous graphitic carbon nitride (g-C_5N_2) catalysts are also systematically screened by using a thermodynamics approach through the *ab initio* density functional theory (DFT) method. Key results include: (a) pristine g-C_5N_2 is most active to catalyze the H_2O/O_2 reaction and produce H_2O_2; (b) the adsorption and activation of water at unsaturated carbon sites of g-C_5N_2 are critical to initiate the H_2O/O_2 reaction, producing HOO* intermediates; (c) interfacial free water and adsorbed water at g-C_5N_2 form a synergetic proton transfer cluster to promote HOO* intermediates to form H_2O_2. To the best of our knowledge, this work presents long-needed theoretical details of direct H_2O_2 synthesis *via* the water/oxygen system, which can guide further optimization of carbon-based catalysts for oxygen reduction reactions.

1. Introduction

Hydrogen peroxide (H_2O_2) has been extensively used for pulp bleaching, wastewater treatment and green oxidization for chemical synthesis.[1–3] With the increasing global demand, how to synthesize H_2O_2 *via* economic and environment friendly processes is a pressing topic. Currently, over 95% of H_2O_2 is produced using an indirect process, involving energy-intensive multistep anthraquinone oxidation and reduction reactions.[1,4] The industrialized process requires a complex and large-scale infrastructure and causes severe pollution to the environment due to the utilization of aromatic chemicals.[5] Since the last decade, direct synthesis of H_2O_2 *via* a two-proton hydrogen/oxygen reaction has attracted much attention.[6,7] Various metal and metal oxide catalysts have been proposed and optimized, among which Pd based alloys and nanoparticles seem to be most promising.[8–11] Unfortunately, this method is limited by the heavy use of strong acids and halides, which would promote metal catalyst leaching and as-produced H_2O_2 requires further purification.[8] In addition, the hydrogen explosion risk at the operational high pressure continues to be a safety hazard and prevents its commercial scale implementation.[12]

Direct H_2O_2 synthesis under ambient conditions, utilizing water as a hydrogen source and combining electrocatalysis or photocatalysis techniques, has witnessed tremendous research efforts recently.[13–17] Kato *et al.*[18] prepared an Fe–Ru bifunctional catalyst to produce H_2O_2 from H_2O and O_2 *via* visible-light photocatalytic reactions. They observed that H_2O adsorption on Fe sites is critical to the following O_2/H_2O reaction. Electrochemically, H_2O_2 synthesis from H_2O and O_2 is a typical two-proton/two-electron ($2H^+/2e^-$) oxygen reduction reaction (ORR).[19] A number of catalysts have been developed with promising efficiency for electrochemical ORR processes, including noble metal-based electrocatalysts (Au,[20] Pt[21] and Pd[17]), single-atom catalysts (Pt@TiN[22]), metal oxide catalysts (Fe_3O_4 (ref. 23) and Mn–Ru oxide[24]) and carbon-based electrocatalysts (N-doped, or B, N co-doped mesoporous carbon[25–28]).

Carbon-based catalysts have been considered as an efficient low-cost, metal-free alternative for green and renewable processes.[29–33] For H_2O_2 synthesis from H_2O and O_2, Cui *et al.*[34] reported that oxidized carbon nanotubes (CNTs) exhibited a higher selectivity and a better activity for the two-electron oxygen reduction reaction. Yang and co-workers[35] found that epoxy and ring ether groups of graphene oxide exhibit an outstanding electrochemical HO_2^- production, achieving a good activity (overpotential <10 mV), an excellent selectivity(≈100%) and a satisfactory stability (over 15 h at

[a]Institute of Industrial Catalysis, College of Chemical Engineering, State Key Laboratory Breeding Base of Green-Chemical Synthesis Technology, Zhejiang University of Technology, Hangzhou 310032, China. E-mail: jgw@zjut.edu.cn

[b]School of Chemical, Biological and Materials Engineering, University of Oklahoma, Norman, Oklahoma 73019, USA. E-mail: HLL@ou.edu

† Electronic supplementary information (ESI) available. See DOI: 10.1039/c9ta08103h

0.45 V in alkaline media). Despite this encouraging progress of carbon-based catalysts for direct H_2O_2 synthesis, detailed fundamental understandings are still incomplete. To just name a few, what is the exact catalytic role of carbon-based materials? what is the critical initial step of H_2O_2 synthesis, water adsorption or oxygen interaction with the catalyst? Is it a one-step reaction or a subsequent two-step proton/electron reaction mechanism? what is the role of the liquid/solid interface?

In this work we report a computational study to reveal the reaction mechanism of direct synthesis of H_2O_2 by a H_2O/O_2 reaction on porous graphitic carbon nitride (g-C_5N_2). Also known as an Aza-fused π-conjugated microporous polymer (Aza-CMP), g-C_5N_2 has a large number of pyridinic nitrogen dopants at zigzag edges, a large surface area, a high pore/volume ratio, and a high electrical conductivity.[36–38] Through a series of AIMD, RxMD and *ab initio* DFT calculations, the following key results have been elucidated: (a) pristine and hydrogenated g-C_5N_2 catalysts have been screened and the most effective catalyst is partially hydrogenated metastable g-C_5N_2; (b) positively charged carbon sites preferentially chemisorb water molecules, which is critical to promote the H_2O/O_2 interaction and generate HOO* intermediates towards H_2O_2 production; (c) a collection of near-surface water molecules could form a proton transfer chain, thus conveniently promoting the reaction of HOO* intermediates to form H_2O_2.

2. Models and simulation methods

2.1 ReaxFF based reactive molecular dynamics simulation

Developed by van Duin and co-workers, the ReaxFF force field provides affordable and accurate atomic details of reactive complex systems.[39,40] With a bond order concept, ReaxFF force field parameters have been fitted to reproduce *ab initio* quantum mechanics calculations. Therefore, ReaxFF based reactive molecular dynamics (RxMD) simulations can describe reaction systems with a similar accuracy to *ab initio* quantum mechanics methods, and effectively handle systems of hundreds of thousands of molecules. The C/N/O/H ReaxFF force field parameters in this work are extracted from the literature.[41] The structural information of g-C_5N_2 has been obtained by both RxMD and *ab initio* DFT calculations. As presented in Fig S1,† the results of characteristic bonds and angles agree quantitatively well with each other. It is also worth noting that RxMD simulations were performed where only 500 water and 25 oxygen molecules were placed in the simulation box at 300.0 K. The simulation results indicated that this process was only a simple physical mix, and no OOH* and H_2O_2 can be observed after 5 ns (Fig. S2†). RxMD simulations were performed with the LAMMPS software package.[42] A canonical ensemble was applied where the number of molecules (N), the volume (V), and the temperature (T) remained constant throughout the calculations. The temperature (300.0 K) was maintained by the Nosé–Hoover method with a damping coefficient of 100.0 fs.[43,44] The initial velocities of water and oxygen molecules were assigned according to the Boltzmann distribution. g-C_5N_2 was treated as a flexible solid substrate during the calculation. Newton's equation was integrated by the velocity Verlet algorithm with a time step of 0.25 fs.[45] A bond-order change of 20% of the original bond length was used to identify the connectivity and molecular species and monitor the system evolution as a function of simulation time.

As illustrated in Fig. 1a, a 2 × 2 supercell was constructed based on the optimized primitive unit cell of g-C_5N_2 containing 30C and 12 N atoms. The simulation box was composed of a single sheet of g-C_5N_2, 68.98 Å (y) × 57.71 Å (x), placed in the middle, and a mixture of 500 water molecules and 25 oxygen molecules, as shown in Fig. 1b. The z dimension of the simulation box was 30.0 Å, so that the interaction between neighboring g-C_5N_2 sheets is negligible. Periodic boundary conditions were applied along the x, y, and z directions. For each RxMD simulation, the system (water, oxygen and g-C_5N_2) was firstly relaxed to optimize the structures, followed by a 2.0 ns calculation to further equilibrate the system. After that, the data were collected for 200 ps for analysis. It is worth noting that there was no restriction on the system: all g-C_5N_2, water and oxygen molecules were allowed to relax and move during the simulation.

2.2 *Ab initio* DFT and *ab initio* MD calculations

Three sets of *ab initio* quantum mechanics calculations have been performed to: (I) screen and evaluate the structural stability of pristine and hydrogenated g-C_5N_2 models; (II) search and reveal H_2O/O_2 reaction mechanism details, such as the transition state, the reaction pathway and the activation energy barrier; (III) generate the reaction trajectory and dynamics properties, to compare with RxMD calculation results, and to identify the two-proton/two-electron ($2H^+/2e^-$) reaction process.

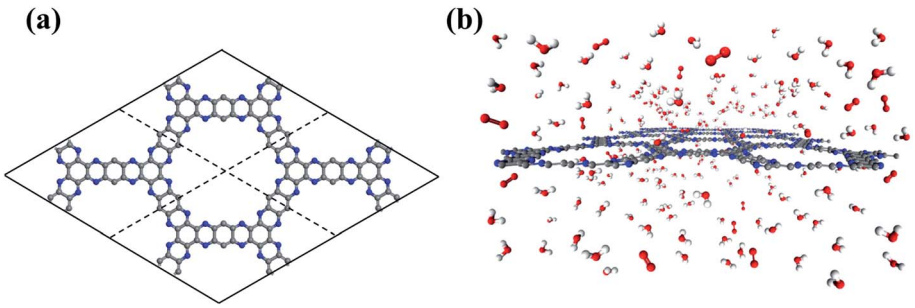

Fig. 1 The illustrations of (a) the initial configurations of a 2 × 2 g-C_5N_2 supercell. (b) The simulation box of g-C_5N_2, H_2O and O_2 molecules.

Geometry optimization and transition state calculation were performed by the *ab initio* DFT method *via* the Vienna *ab initio* simulation package (VASP).[46–48] The exchange-correlation functional was treated *via* the generalized gradient approximation (GGA) method with Perdew–Burke–Ernzerhof (PBE).[49] Empirical D3 Grimme's method (DFT-D3) was adopted to improve the description of van der Waals interactions in all calculations.[50] The planewave kinetic energy cutoff was 450.0 eV. Geometries were optimized until the residual forces were smaller than 0.05 eV $Å^{-1}$. A $5 \times 5 \times 1$ grid was used for *k*-point sampling, according to the Monkhorst–Pack method.[51] A vacuum of 20.0 Å was added to the *z* direction to avoid mirror image interactions. The climbing image-modified nudged elastic band (CI-NEB) method was used to evaluate the activation energies of different reaction paths.[52] A total of 55 g-C_5N_2 models were generated to represent pristine and all possible hydrogenations in terms of coverage and distribution of hydrogen atoms. Optimized structures and the corresponding equilibrium energies are summarized in Fig. S3 and Table S1 of the ESI.†

Ab initio molecular dynamics (AIMD) calculations were performed by using the CP2K package.[49,53] The system (g-C_5N_2, water and oxygen) was maintained at 300.0 K using the canonical (NVT) ensemble, where the temperature was controlled *via* the Nosé–Hoover thermostat.[43,54] Each calculation was performed for 2.0 ps with a time step of 0.25 fs. The wave functions were expanded in an optimized double-ζ Gaussian basis set.[55] The electrostatic energy cutoff for an auxiliary plane wave basis set was 360.0 Ry.[56] Van der Waals interactions were corrected by the Grimme algorithm (DFT-D3).[50]

2.3 Choice of three simulation methods

While the overall goal of this work is to reveal how water and oxygen react on a carbon nitride catalyst (g-C_5N_2) to produce hydrogen peroxide, the thermal stability of the catalyst and the diffusion/reaction coupled complex process are worth exploring. Thus, we take advantage of three adopted simulation methods to understand the system. First of all, to mimic experimental g-C_5N_2 and provide insight into catalyst screening and optimization, a series of *ab initio* DFT calculations were performed to calculate the Gibbs free energy and evaluate the thermal stability of all g-C_5N_2 models. Secondly, it is critical to understand the first step of the reaction, the energy barrier and the reaction pathway. Thus, *ab initio* quantum mechanics methods are appropriate choices. Along this direction, we have performed *ab initio* DFT and AIMD calculations. Thirdly, H_2O_2 synthesis is a complex process and it occurs at the gas/liquid/solid interface. Obviously, the adsorption and diffusion of reactants (H_2O and O_2) to the solid interface (g-C_5N_2) could be significant parameters. Additionally, after the synthesis reaction, the competitive desorption of H_2O_2 from the solid interface is also vital to a successful separation and purification of the H_2O_2 product. The ReaxFF potential has become a powerful computational tool to explore the chemisorption and reactions of complex systems. More importantly, RxMD simulations not only can describe systems composed of hundreds of thousands of atoms but also can archive a trajectory to the time sale of microseconds. Therefore, RxMD was adopted to study such a complex and multiscale system. The three methods complement each other and provide insights from different perspectives.

3. Results and discussion

3.1 Gibbs free energy calculation and thermal stability of g-C_5N_2 models

The stability of 55 g-C_5N_2 models was firstly investigated by the *ab initio* DFT based thermodynamics approach.[57–59] The most stable model generally has the lowest Gibbs free energy. In this work, the surface energy (Ω) is calculated according to eqn (1):[60,61]

$$\Omega(T, P_i, N_i) = \frac{1}{2A}\left(G(T, P_i, N_i) - \sum_i N_i\mu_i(T, P_i)\right) \quad (1)$$

where A and G are the surface area and Gibbs free energy of the g-C_5N_2 model, respectively; μ_i is the overall chemical potential of a total number of N_i atoms or molecules of species i. T is the temperature; P is the hydrogen partial pressure. For the solid phase, the change of P has a negligible effect on the Ω value. Thus, eqn (1) could be expressed as:

$$\Omega(T, P_i, N_i) = \frac{1}{2A}\left(E_{g\text{-}C_5N_2H} - E_{g\text{-}C_5N_2} - N_H\mu_H\right) \quad (2)$$

where $E_{g\text{-}C_5N_2H}$ and $E_{g\text{-}C_5N_2}$ are respectively the total energy of hydrogenated g-C_5N_2 and pristine g-C_5N_2 from *ab initio* DFT calculations; N_H is the number of hydrogen atoms of the g-C_5N_2 model; μ_H is the chemical potential of a single hydrogen atom, which is approximated by the chemical potential of a gas-phase hydrogen molecule:

$$\mu_H = \frac{\mu_{H_2}^{gas}}{2} \quad (3)$$

At the studied temperature of 300.0 K, the gas-phase hydrogen could be treated as an ideal gas. Therefore, the chemical potential could be calculated by using eqn (4):

$$\mu_{H_2}^{gas}(T, P_{H_2}) = \mu_{H_2}^{gas}(T, P^0) + kT\ln\left(\frac{P_{H_2}}{P^0}\right) = \mu_{H_2}^{gas}(T^0, P^0) + \Delta G_{H_2}^{gas}(T, P^0) + kT\ln\left(\frac{P_{H_2}}{P^0}\right) \quad (4)$$

where $\mu_{H_2}^{gas}(T^0, P^0)$ is the chemical potential of the hydrogen molecule in the standard state (T^0 = 298.15 K, P^0 = 1 atm), $kT\ln\left(\frac{P_{H_2}}{P^0}\right)$ is the pressure-dependent term. $\Delta G_{H_2}^{gas}(T, P^0)$ is the temperature-dependent term, referring to the Gibbs free energy change when the temperature changes from T^0 = 298.15 K to T = 300.0 K (see Table S2†), while keeping the pressure at P^0:

$$\Delta G_{H_2}^{gas}(T, P^0) = G_{H_2}^{gas}(T, P^0) - G_{H_2}^{gas}(T^0, P^0) \quad (5)$$

The chemical potential of the hydrogen molecule under standard state conditions is:

$$\mu_{H_2}^{gas}(T^0, P^0) = H_{H_2}^0 - T^0 S_{H_2}^0 \quad (6)$$

where $S^0_{H_2}$ is obtained from the NIST thermodynamic tables,[62] and $H^0_{H_2}$ is calculated using experimental data of heat of formation of water:

$$H^0_{H_2} = H^0_{H_2O} - \frac{1}{2}H^0_{O_2} - \Delta H^0_{f,H_2O} \quad (7)$$

where the enthalpies of $H^0_{O_2}$ and $H^0_{H_2O}$ are adopted from the literature. The oxygen gas entropy $S^0_{O_2}$ in the standard state is from experimental data. Hence, eqn (2) and (3) yield:

$$\mu_H = 0.5H^0_{H_2O} - \frac{1}{2}H^0_{O_2} - \Delta H^0_{f,H_2O} + \Delta G^{gas}_{H_2}(T, P^0) + kT\ \mathrm{In}\left(\frac{P_{H_2}}{P^0}\right) \quad (8)$$

$$\Omega(T, P_i,\ N_i) = \frac{1}{2A}\left\{E_{C_5N_2H} - E_{C_5N_2H} - 0.5N_H\left[H^0_{H_2O} - \frac{1}{2}H^0_{O_2} - \Delta H^0_{f,H_2O} + \Delta G^{gas}_{H_2}(T, P^0) + kT\ \ln\left(\frac{P_{H_2}}{P^0}\right)\right]\right\} \quad (9)$$

As shown in Fig. S3 and Table S1,† the proposed models are constructed based on the degree of hydrogenation, that is, the number of hydrogen atoms added to pristine g-C_5N_2. When multiple candidates exist for a same degree of hydrogenation, the most stable model (with the lowest Gibbs free energy) is then selected as the representative one. With this information, 19 out of the total 55 possible g-C_5N_2 models were selected for the Gibbs free energy calculation to evaluate their thermal stability. The calculations were performed under atmospheric conditions, as a function of variation of hydrogen chemical potential from −0.58 eV to −1.10 eV, which corresponds to the temperature range of 300.0 to 1100.0 K. As shown in Fig. 2a, the Gibbs free energy was expressed as a function of temperature at a fixed partial pressure of hydrogen, P_{H_2} = 1 atm. A more negative Gibbs free energy indicates a better thermal stability of the g-C_5N_2 model. In addition, the negative slope suggests that the thermal stability generally declines when the temperature increases. According to the Gibbs free energy calculation, the hydrogen coverage (*i.e.*, the degree of hydrogenation) affects the thermal stability. But the dependence is not linear according to the results in Fig. 2a. This is probably due to different activities of C and N sites of g-C_5N_2. The same degree of hydrogenation could have different hydrogen distributions from C and N sites.

In this work, we selected five models to study their catalytic roles in H_2O_2 synthesis. As illustrated in Fig. 2b, the models represent respectively pristine (Model 1, no hydrogenation), C-site full hydrogenation (Model 2), N-site full hydrogenation (Model 3), full hydrogenation (Model 4, both C and N sites hydrogenated), and partial hydrogenation (Model 5, C sites fully and N sites partially hydrogenated), which is the most stable model from the Gibbs free energy calculation. The electron localization function (ELF) analysis in Fig. 2c shows the distribution of electrons of the models, where sites with higher electron densities (red color) are preferential to interact with H_2O and O_2 molecules.

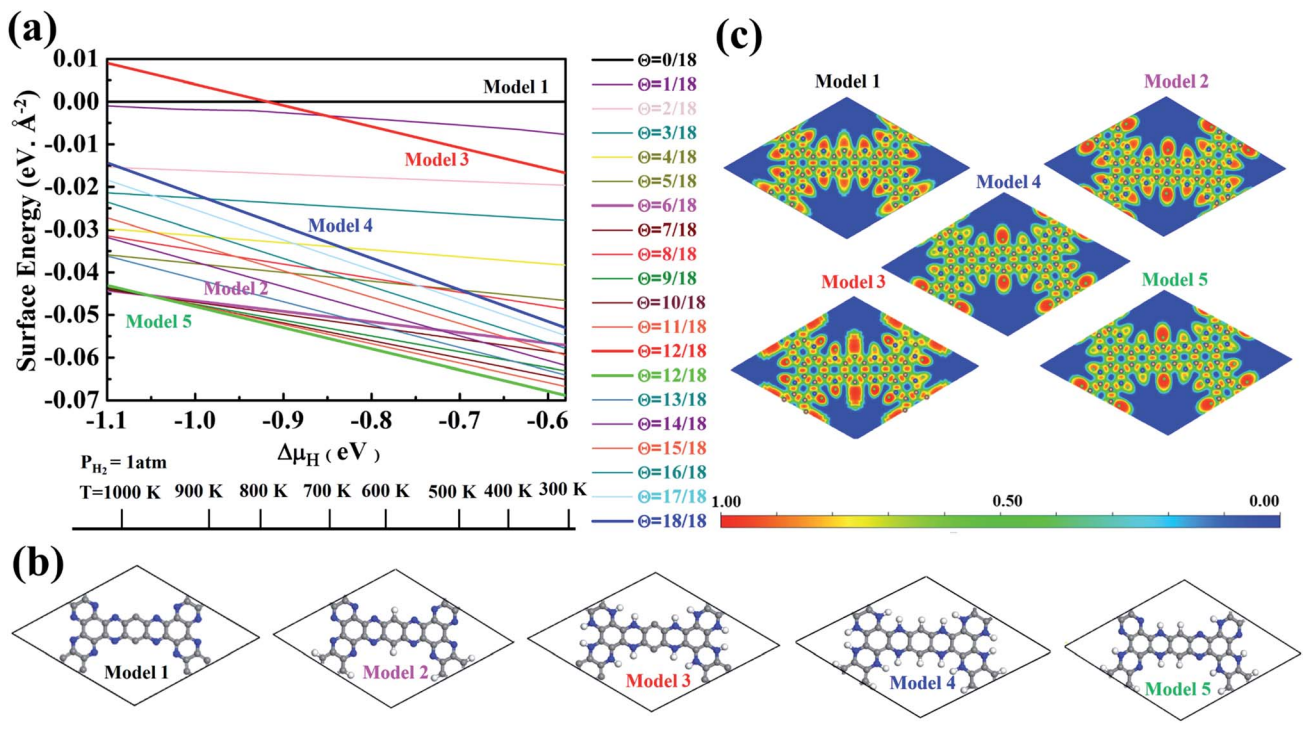

Fig. 2 Calculations of the thermodynamic stability and electronic structure. (a) Phase diagrams: the regions of stability of g-C_5N_2 surfaces with different terminations as a function of hydrogen chemical potential variations. (b) Five selected model structures of g-C_5N_2. (c) Electronic localized function (ELF) analysis of the five models. For the scale bar of 0.0 to 1.0, the red region indicates a higher local electron distribution, the green region represents electronic-gas-like pair probability and the blue region shows a higher electronic delocalized distribution.

3.2 Preferential water adsorption on g-C_5N_2

In order to elucidate which reactant (H_2O or O_2) initiates the reaction, the H_2O/g-C_5N_2 and O_2/g-C_5N_2 systems have been studied separately with the pristine Model 1. *Ab initio* DFT calculations reveal that O_2 and H_2O adsorption at the pores of g-C_5N_2 has stronger binding energies than that of the basal plane of g-C_5N_2 (Fig. S4†). The adsorption energy is respectively −1.68 eV and −1.14 eV for H_2O/g-C_5N_2 and O_2/g-C_5N_2 at the unsaturated C site, suggesting a preferential interaction between H_2O and g-C_5N_2. The comparison was performed using RxMD simulations where 500H_2O molecules or 50O_2 molecules were placed to interact with pristine g-C_5N_2 (Model 1) at 300.0 K. For the O_2/g-C_5N_2 system, only 4 O_2 molecules were adsorbed at unsaturated C sites. No preferential interaction between O_2/N sites was observed, see Fig. S5 of the ESI.† Meanwhile, for the H_2O/g-C_5N_2 system, as shown in Fig. 3a, water was preferentially distributed to form an ordered ring configuration along the pores of pristine g-C_5N_2. This phenomenon was also observed *via ab initio* DFT calculation. A zoom-in snapshot of Fig. 3b clearly reveals three types of water molecules in the system, namely, adsorbed water at unsaturated C sites, water molecules near g-C_5N_2 which form a hydrogen bonding network with adsorbed water, and bulk water not shown in Fig. 3b for clarity. The Bader charge analysis in Fig. S6† demonstrates that uncoordinated carbon of pristine g-C_5N_2 carriers a positive charge of 0.18 e by average. This confirms that positively charged carbon of g-C_5N_2 interacts strongly with water through its negatively charged oxygen atom.

The distributions of water near C and N sites are shown in Fig. 3c and d, respectively. In Fig. 3c, the first two peaks around 1.50 Å are from absorbed water. As illustrated in Fig. 3b, adsorbed water generally adopts the 'v' configuration, atop of C sites. The adsorbed water still demonstrates a certain degree of freedom, which results in two close peaks at 1.50 Å. The peaks around 2.5 Å and 3.7 Å come from hydrogen-bonded water molecules. Limited by the pore size of g-C_5N_2, diameter ~13.82 Å, only two layers of hydrogen bonds (HB) are allowed, as illustrated by the dotted circles in Fig. 3b. The distribution analysis around N sites revealed one significant peak at around 2.97 Å, which represents hydrogen bonds between two adsorbed water molecules. Due to the negative charge, hydrogen of water stays closer to the N sites, at 2.38 Å.

3.3 Reaction mechanism for direct H_2O_2 synthesis

A series of RxMD and AIMD simulations have been performed to reveal the reaction mechanism of H_2O and O_2 on g-C_5N_2 catalysts and the complete process of direct H_2O_2 synthesis. Fig. 4 presents key snapshots of a representative RxMD simulation, demonstrating how one H_2O_2 molecule was synthesized by a two-step reaction of H_2O/O_2 on pristine g-C_5N_2 (Model 1). It

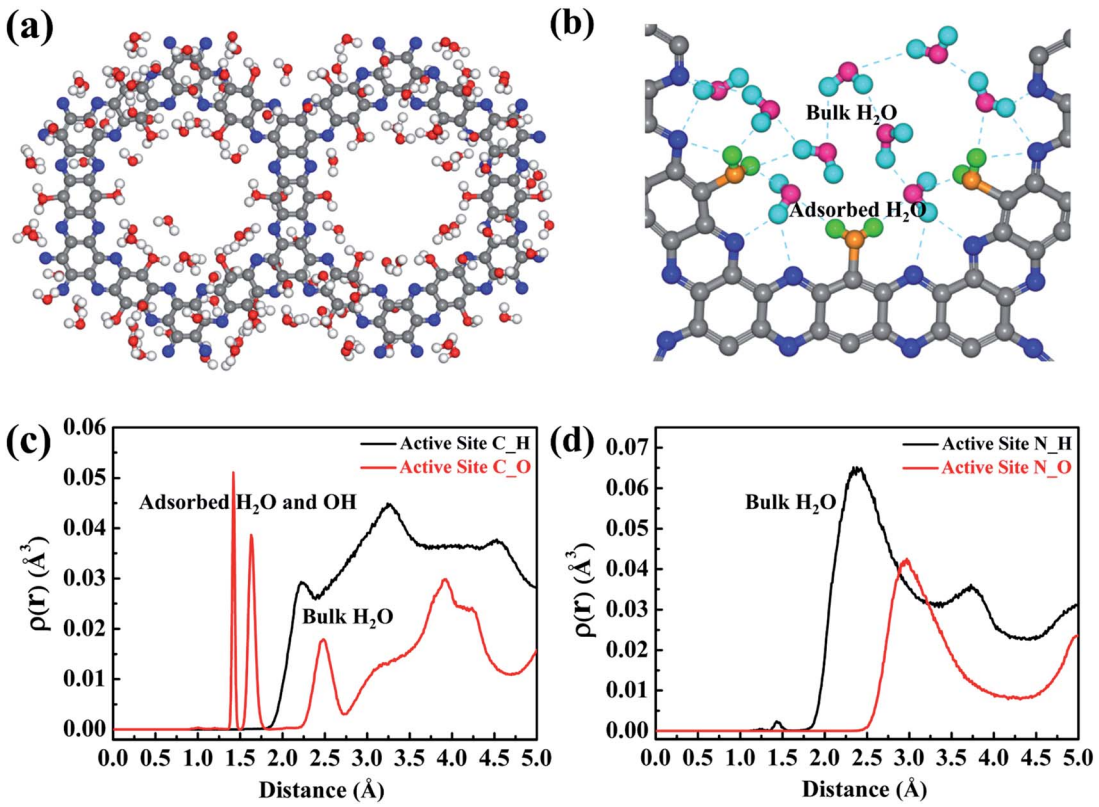

Fig. 3 (a) The distribution of water molecules in the pores of dehydrogenated g-C_5N_2. (b) The distribution of water molecules, including adsorbed and bulk H_2O. The atomic density distribution for the water molecule on (c) the C site and (d) the N site. The color codes are: C of g-C_5N_2, gray; N of g-C_5N_2, blue; H of free H_2O, cyan; O of free H_2O, pink; H of adsorbed H_2O, green; O of adsorbed H_2O, yellow. Both line and ball models are used in the snapshots, to emphasize the formation of H_2O_2. For clarity, not all free water molecules are shown.

is worth noting that during the RxMD simulation, oxygen and hydrogen were assigned different colors to facilitate tracking of the reaction progress: adsorbed water, oxygen-yellow and hydrogen-green; near surface HB bonded water, oxygen-pink and hydrogen-turquoise; gas-phase oxygen-red. As shown in Fig. 4, step 1 illustrates a critical configuration where water molecules were adsorbed at unsaturated C sites of the pore, and gas-phase oxygen molecules were closer to adsorbed water. From step 1 to step 3, the interaction between O_2 and adsorbed water was witnessed by the OH bond length, changing from 2.037 Å to 1.591 Å, and eventually leading to the dissociation of the adsorbed water and the formation of the OOH* intermediate.

Snapshots from step 4 to step 6 revealed an interesting proton exchange mechanism involving the newly generated OOH* intermediate, a nearby water molecule and another adsorbed water molecule from the neighboring C site. While the overall result is that one oxygen molecule interacts with two adsorbed water molecules to directly synthesize one H_2O_2 molecule, the snapshot of step 6 clearly shows that the two hydrogen atoms of the H_2O_2 molecule came from two different proton donors, which is convincing evidence of the proton exchange event involving near surface water molecules.

It is interesting to note that a different reaction mechanism was also observed from the simulation trajectory, where the O_2 molecule interacted successively with two adsorbed H_2O molecules. As shown by the trajectory snapshots in Fig. 5, the configuration of step 2 is critical: the O_2 molecule diffused to the location where it could simultaneously interact with two adsorbed water molecules. The HOO* intermediate was then produced as a result of the interactions. In addition, since the intermediate was still very close to the other adsorbed water molecule, it could receive the second proton and lead the reaction to completion to produce one H_2O_2 molecule. The color of hydrogen atoms of H_2O_2, step 6 in Fig. 5, clearly demonstrates that no free or hydrogen bonded water participated in the two-step reaction process.

The snapshots shown in Fig. 6 are from the AIMD calculation of 5 O_2 molecules, 20H_2O molecules and a pristine g-C_5N_2 model. It is worth noting that, due to the high computational cost, there were fewer oxygen and water molecules in the AIMD calculations. But both RxMD and AIMD were performed at 300.0 K with the same g-C_5N_2 model. The analyses of AIMD and RxMD trajectories give the same conclusion, that is, the first critical step is H_2O adsorption at edge unsaturated C sites, followed by O_2 interaction with adsorbed water to form a HOO* intermediate. Then, different hydrogen suppliers can interact with HOO* to produce H_2O_2. Simultaneously, the interaction between adsorbed water and nearby water molecules was also observed, sequentially producing a hydronium ion (H_3O^+, step 5) and then a Zundel cation ($H_5O_2^+$, step 6). H_2O_2 was eventually synthesized as a reaction product between HOO* and $H_5O_2^+$, as illustrated by steps 8 and 9 in Fig. 6. As the reaction proceeded, OH* or O* would be accumulated on the unsaturated edge-C sites. It is probably challenging to regenerate g-C_5N_2 by the H_2O/O_2 system as used in this work. However, convenient techniques are available to recycle the catalyst. Removing OH*/O* and regenerating active sites of carbon-based catalysts can be achieved by electrocatalytic reactions. For example, for 4-electron ORR processes,[63–65] adsorbed OH* is hydrogenated and

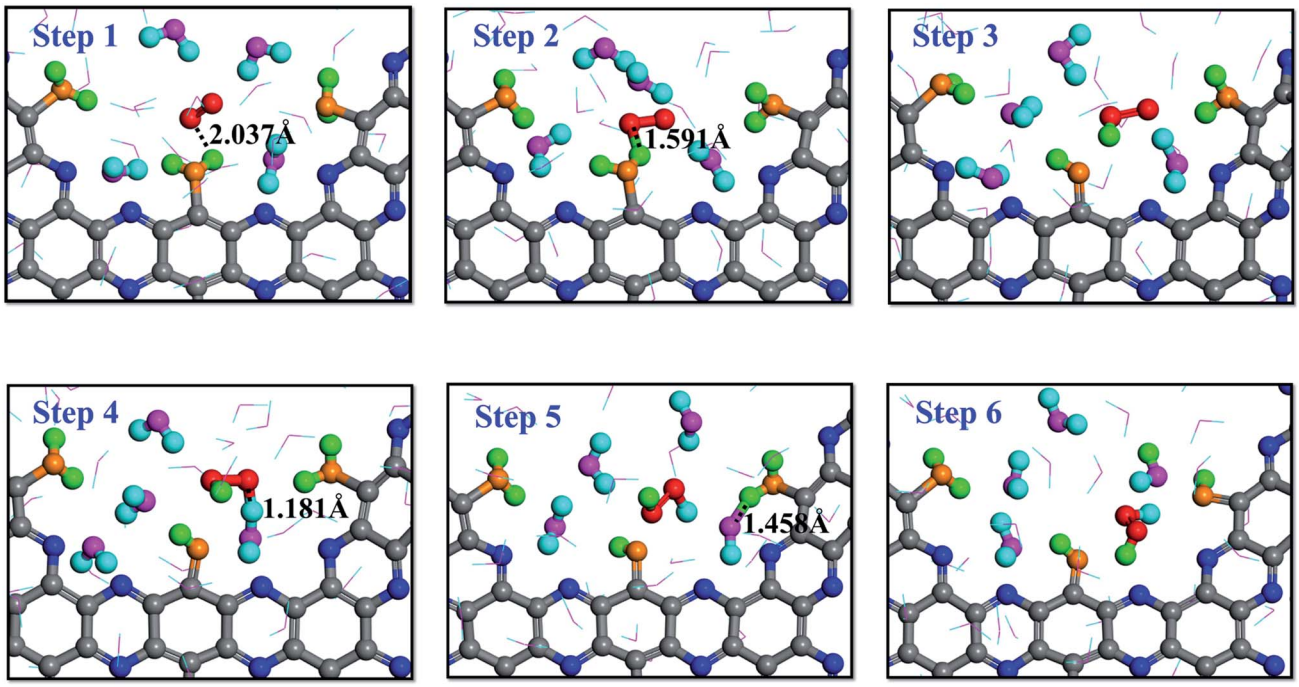

Fig. 4 Proton transfer mechanism (PTM) on the dehydrogenated g-C_5N_2 system: the hydrogen atoms of H_2O_2 come from adsorbed water and bulk water, respectively.

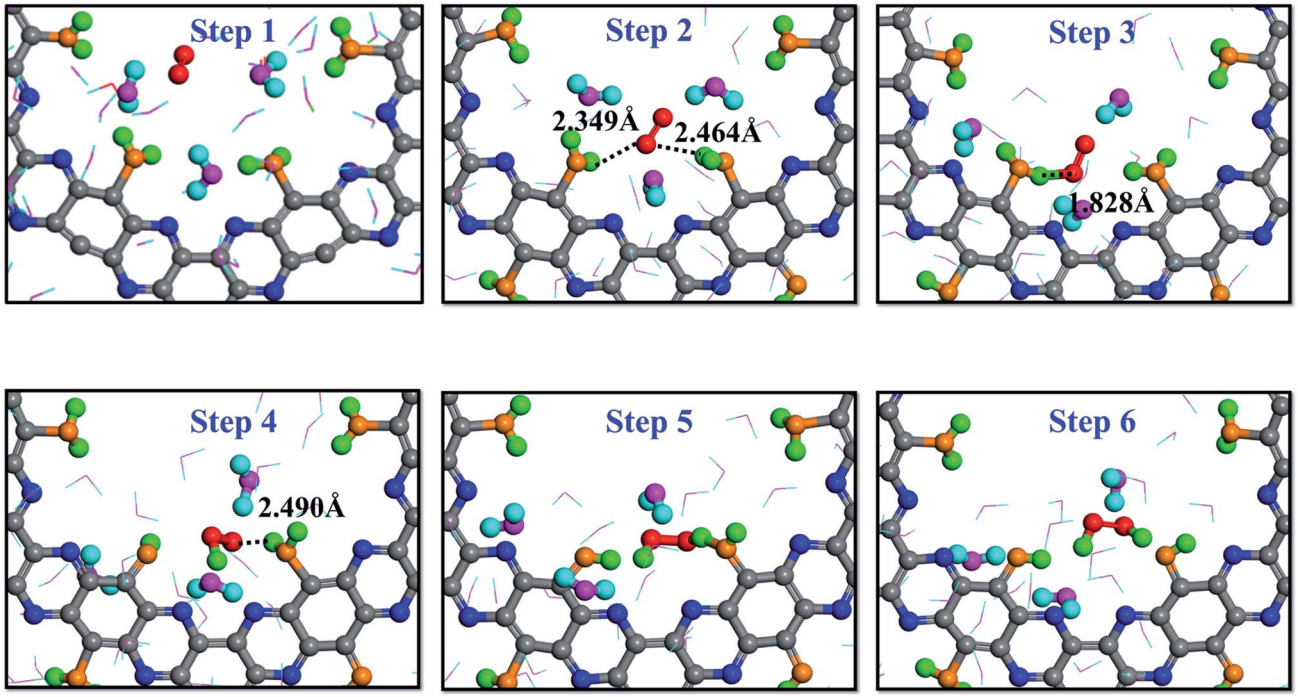

Fig. 5 Direct formation mechanism (DFM) on the dehydrogenated g-C_5N_2 system: the H atoms of H_2O_2 both come from adsorbed H_2O.

removed in the form of H_2O. Liang and co-workers studied the 4-electron ORR of nitrogen doped graphene (N-graphene). Their results demonstrated that the removal of adsorbed OH* from the N-graphene surface that is covered by O with a 1/6 monolayer surface oxygen coverage has a small energy barrier of 0.32 eV in the water solution phase.[66] The regeneration depends closely on the form of deactivated g-C_5N_2 catalysts, the concentration of H_3O^+ and the applied voltage. To validate the general regeneration process, a proof-of-concept calculation is designed in this work, to mimic a separate electrocatalytic treatment after the successful H_2O_2 production, to remove surface OH and O groups and regenerate the active carbon sites of g-C_5N_2. As shown in Fig. S7(a),† six H_2O and two H_3O^+ molecules are placed at the pore of the deactivated g-C_5N_2 where its edge nitrogen sites are fully hydrogenated and carbon sites are alternatively bonded with OH and O. The AIMD simulation results in Fig. S7(b) and (c)† show that within 0.2 ps H_3O^+ interacts with oxygen-containing functional groups at edge carbon sites, transforming OH* and O* back to adsorbed water at edge carbon sites, thus regenerating the g-C_5N_2 catalyst for the next cycle of H_2O_2 production.

Both RxMD and AIMD reveal the same overall reaction mechanism which can be generally described by two sequential steps: (a) the formation of HOO* intermediates, from the interactions between oxygen and adsorbed water; (b) the completion of H_2O_2 synthesis, by the proton transfer between HOO* and chain-cluster water (or second adsorbed water); (c) H_2O* regeneration, by interactions between residual OH* and H_3O^+ molecules. The key steps are summarized below:

H_2O adsorption:

$$H_2O_{(bulk)} + \text{g-}C_5N_2 \rightarrow \text{g-}C_5N_2\ {}^*H_2O_{(ad)} \quad (R1)$$

HOO* formation:

$$O_{2(gas)} + H_2O_{(ad)} \rightarrow HOO^*_{(bulk)} + {-}OH_{(dec)} \quad (R2)$$

H_2O_2 formation:

$$HOO^*_{(bulk)} + H_2O_{(chain)} \rightarrow H_2O_{2(bulk)} + {-}OH_{(dec)} \quad (R3.1)$$

$$HOO^*_{(bulk)} + {}^*H_2O_{(ad)} \rightarrow H_2O_{2(bulk)} + {-}OH_{(dec)} \quad (R3.2)$$

H_2O chain:

Hydronium ion: $${}^*H_2O_{(ad)} + H_2O_{(bulk)} \rightarrow H_3O^+_{(bulk)} + {-}OH_{(dec)} \quad (R3.1a)$$

Zundel cation: $$H_3O^+_{(bulk)} + H_2O_{(bulk)} \rightarrow H_5O_2{}^+_{(bulk)} \quad (R3.1b)$$

H_2O* regeneration: $$OH^* + H_3O^+_{(bulk)} \rightarrow H_2O_{(ad)} + H_2O_{(bulk)} \quad (R4)$$

For other studied g-C_5N_2 models where N- or C-sites are hydrogenated, H_2O_2 was produced by a similar reaction mechanism. The complete process was recorded for a few H_2O_2 molecules, as shown in Fig. S8–11.† Hydrogenated N-sites (Model 3 and Model 4) are potential proton providers. Different H_2O_2 molecules have been identified from the calculations: (a) H_2O_2 synthesized by interacting with an absorbed water and a hydrogenated N-site (Model 3), Fig. S8;† (b) H_2O_2 synthesized by receiving two hydrogens from the same adsorbed water

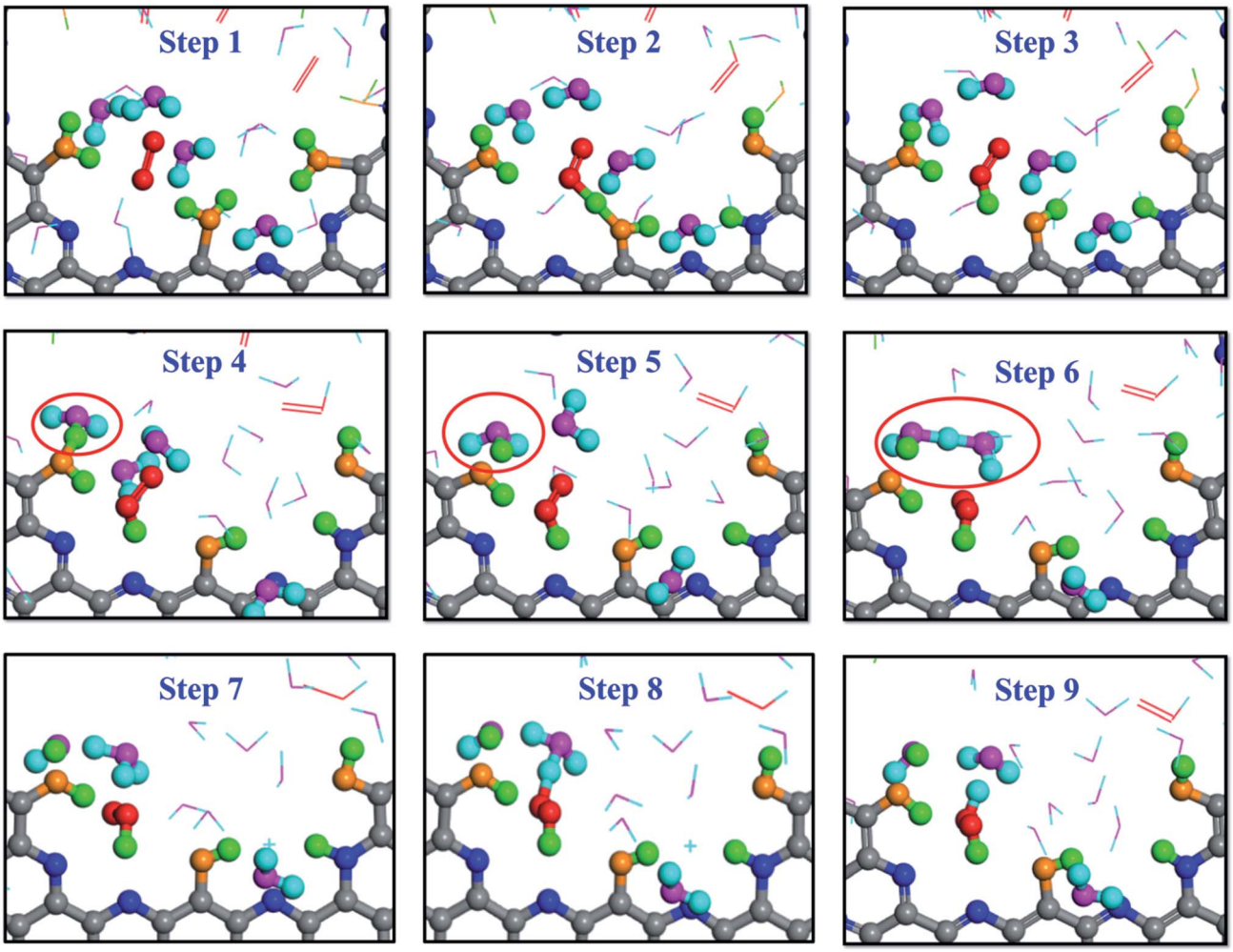

Fig. 6 Snapshots of H_2O_2 production on dehydrogenated g-C_5N_2 described by the AIMD simulations. Structures corresponding to the reaction path followed by PTM.

molecule (Model 3), Fig. S9† (c) H_2O_2 synthesized by interacting with an absorbed water and a hydrogenated N-site, *via* a H_2O proton transfer chain (Model 4), Fig. S10;† (d) H_2O_2 synthesized by directly interacting with two hydrogenated N-sites (Model 4), Fig. S11.† Goclon and Winkler[67] reported that the oxygen reduction proceeds through a one-step two-electron direct process with a 2.15 eV energy barrier on the amino functionalized g-C_3N_4 structure. In contrast, for the hydrogenated g-C_3N_4 catalyst, the two-step single-electron indirect H_2O_2 synthesis has an energy barrier of 1.78 eV. This indicates that the O_2 molecule can directly interact with hydrogenated sites to produce H_2O_2.

Both RxMD and AIMD calculations confirm the direct H_2O_2 synthesis from chemisorbed water and gaseous colliding oxygen molecules, which is known as the Eley–Rideal (ER) reaction. A direct ER reaction is generally expected to occur only when there is a rather small activation barrier to the reaction, such as a gas-phase radical reactant which undergoes an exothermic reaction. In this work, we adopted the CI-NEB method to study the reaction pathway and activation energy for producing HOO* intermediates and H_2O_2.

As shown in Fig. 7a, for the HOO* intermediate, the initial configuration in the system has a gaseous O_2 and one adsorbed H_2O molecule at g-C_5N_2. While the final configuration has a HOO* intermediate and OH-functionalized g-C_5N_2. For the initial configuration, upon water adsorption at the unsaturated C sites, the O–H bond was elongated, changing from 0.972 Å of the bulk to 1.110 Å. The transition state was identified in which the gaseous O_2 was interacting with the adsorbed water, to the extent that the adsorbed water has two equally elongated O–H bonds, one with the gaseous O_2 and the other from the adsorbed water. The calculation revealed that the activation energy (E_{act}) for HOO* formation was 0.23 eV, and the overall reaction was exothermic, releasing 0.91 eV from the system. The exothermic nature indicates that the proton transfer from adsorbed water to a nearby O_2 molecule is energetically favored.

Fig. 7b shows the reaction pathway by which the HOO* intermediate received the second proton to generate a H_2O_2 molecule. As revealed by RxMD and AIMD calculations, this reaction generally involves 'free' water molecules to transfer protons from adsorbed water. It was also observed, see Fig. 5, that the gaseous O_2 could interact successively with two

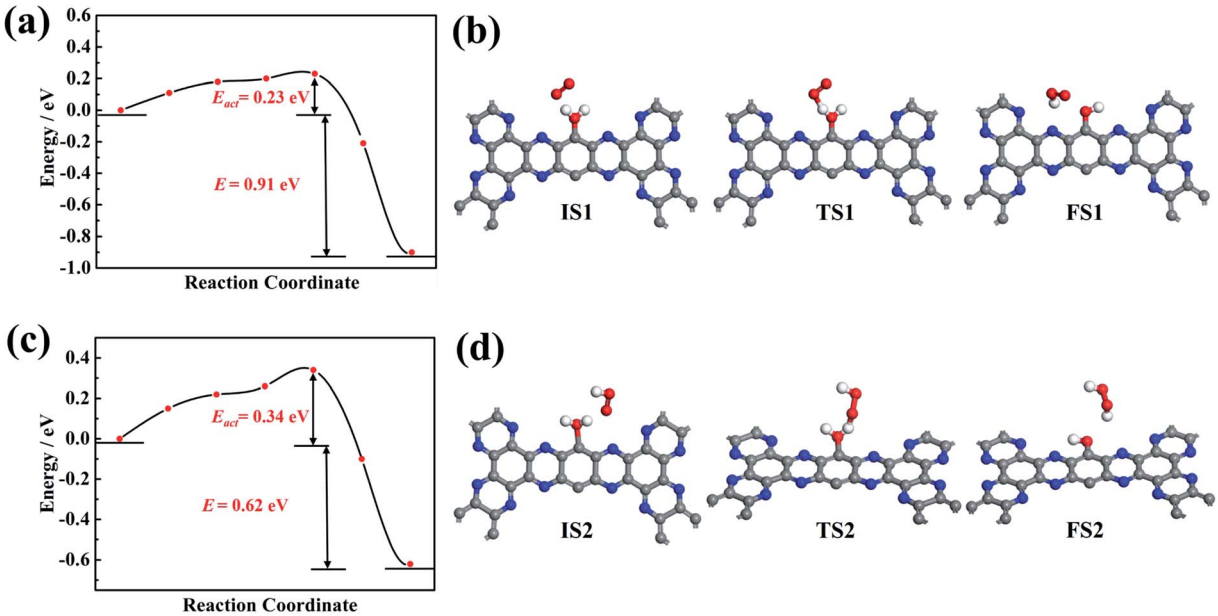

Fig. 7 Energy profile and optimized configurations for OOH* and H_2O_2 formation. (a) and (c) Energy profile for OOH* and H_2O_2 formation by DFT calculation, respectively; (b) and (d) the optimized initial state, transition state and final state configurations for OOH* and H_2O_2 formation, respectively.

adsorbed H_2O molecules to produce a H_2O_2 molecule, which does not require much diffusion of the HOO* intermediate. It is also worth pointing out that there is no 'free' water considered in the CI-NEB calculations, and only the direct reaction between HOO* and adsorbed water to form H_2O_2 was calculated. The result suggested that a larger activation energy (0.34 eV) was necessary to overcome the reaction barrier. But the overall reaction was also exothermic, discharging 0.63 eV from the system.

3.4 Proton transfer along hydrogen bonds

Proton transfer is essential to many aqueous processes, from ion channel function to enzymatic reactions.[68–70] Especially for photocatalytic[71,72] and electrocatalytic reactions,[73,74] simultaneous gain or loss of electrons and protons frequently occur in aqueous solutions. Nevertheless, not enough emphasis has been placed on the effect of proton transfer in aqueous reactions. Experimentally, direct observation of proton transfer is challenging due to the short lifetime of intermediates and the difficulty of distinguishing protons, electrons and their coupling with solvent molecules. For example, Yu and co-workers[75] investigated the Langmuir–Hinshelwood (LH) and ER mechanisms for the ORR on graphene sheets. They performed *ab initio* DFT calculations to mimic ER reactions under an alkaline environment, with H shuttling through one or two water molecules. Other theoretical efforts of understanding proton transfer mechanisms have been summarized in recent reviews.[76–85] It has been demonstrated that the proton transfer can largely determine the energy profile and reaction pathway. However, as far as we are aware, there is no quantitative description of proton transfer in ORR processes.

Here, we propose a proton transfer descriptor based on the structural information of involved water molecules. As illustrated in Fig. 8a, the descriptor δ describes the geometric requirement, assuming that proton transfer occurs when the oxygen atoms of water molecules have three identical hydrogen atoms nearby. Therefore, breaking O–H bonds and exchanging hydrogen atoms (protons) require a negligible energy penalty. The δ value is estimated by using the equation:

$$\delta = \frac{\theta_1}{\theta_0} + \frac{\theta_2}{\theta_0} + \frac{L_1}{L_0}$$

where θ_0 and L_0 are respectively the equilibrium angle and bond length of free H_2O molecules; θ_1 and θ_2 are the new angles, namely H_1–O–H_3 and H_2–O–H_3 according to Fig. 8a, formed between two nearby water molecules; L_1 is the distance between the oxygen atom and the potential exchangeable H_3 hydrogen (proton). Mathematically, δ reaches a minimum whenever there is a proton transfer event.

Previous studies observed Eigen ($H_9O_4^+$)[86,87] and $H_5O_2^+$ (ref. 88) evolution from bulk water. This suggests that proton transfer events involving two or three water molecules are energetically favorable. In this work, dehydrogenated carbon sites provide localized positive charge centers, which promote H_2O adsorption and subsequent $H_5O_2^+$ ion formation (Fig. 8b). Representative snapshots in Fig. 8b demonstrate how near-surface water molecules participate in proton transfer events and promote the HOO* intermediate to receive a proton and thus produce H_2O_2. The AIMD trajectory reveals that two bulk water molecules are involved in this proton transfer process (Fig. 8b(I)): firstly, as shown in Fig. 8b(II), the adsorbed H_2O interacted with a nearby bulk H_2O molecule to form a hydronium H_3O^+ and an OH functional group of g-C_5N_2, and after

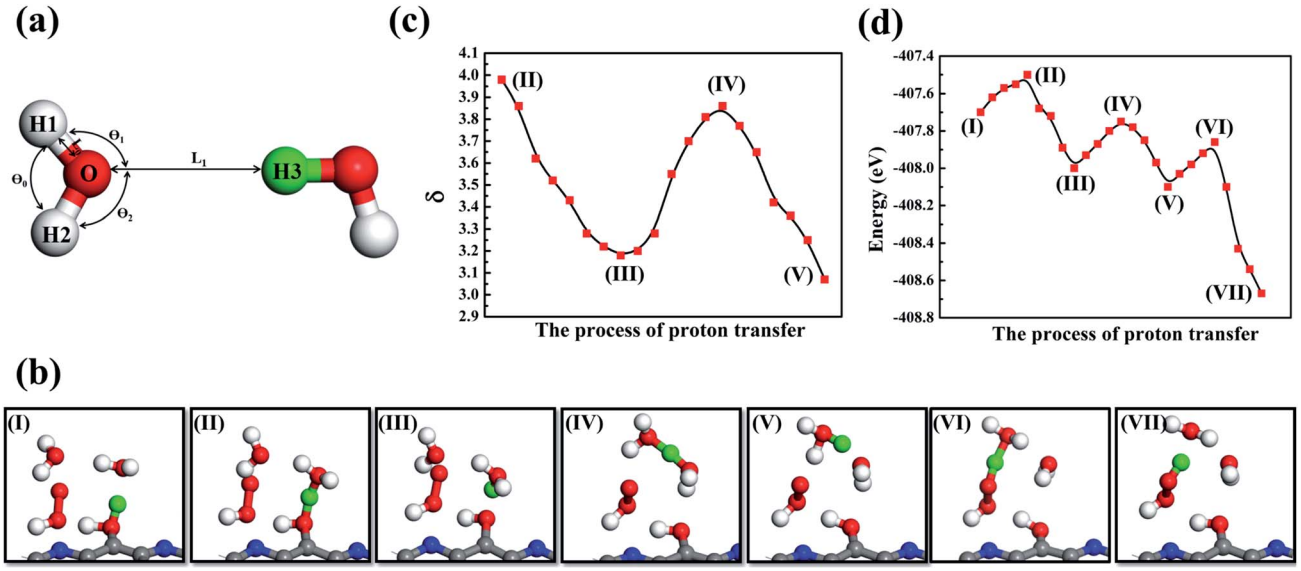

Fig. 8 Proton transfer *via* a chain of water molecules. (a) Schematic representation of the proton transfer process. (b) Trajectory snapshots (I–VII) of critical configurations to the proton transfer for H_2O_2 production. (c) and (d) The change of φ and the total energy in the process of proton transfer, respectively. The dissociated proton exists as a Zundel ion and a hydrated hydronium ion in the systems. C, O, H and N atoms are colored gray, red, white and blue, respectively. The H atom of the adsorbed water that participates in the proton transfer is colored green to guide the viewing.

that the adsorbed water gave up the proton (green color), see Fig. 8b(III). The hydronium H_3O^+ then interacted with another bulk water molecule to form a $H_5O_2^+$ cation, as shown in Fig. 8b(IV). It is worth noting that the oxygen–oxygen distance, between the second bulk water molecule and the previously formed H_3O^+, is about 2.70 Å which is within a typical hydrogen bond cutoff.[89] This suggests that the second water molecule could easily accept a hydrogen atom from H_3O^+, forming a new hydronium H_3O^+, see Fig. 8b(V). Since the new H_3O^+ was much closer to the HOO* intermediate, it easily gives up a proton to HOO* to promote the formation of H_2O_2 (Fig. 8b(VI and VII)). Additionally, direct proton exchange was also observed between adsorbed H_2O molecules and g-C_5N_2, see Fig. S12.†

It has been reported[89] that a Zundel proton is formed when two water molecules, the oxygen–oxygen distance, are within 1.35 Å. To quantify proton transfer events, we adopted the same cut-off of 1.35 Å to determine whether a proton transfer event could occur between two water molecules. In addition, since the four atoms of the hydronium ion H_3O^+ adopt a trigonal pyramidal geometry, an angular term is necessary to describe proton transfer events. Using the definition of φ, the dynamics trajectory was monitored. As shown in Fig. 8b, in the process of forming the first H_3O^+, the value of the bulk and adsorbed H_2O molecules gradually decreases (II to III), eventually reaching the minimum where the bulk water molecule accepted a proton from the adsorbed water, forming H_3O^+. From (III to IV) of Fig. 8b, the H_3O^+ interacted with a second water molecule, firstly forming the Zundel proton $H_5O_2^+$, where increased to reach the maximum at (IV). The value then decreased and reached the minimum again, where the $H_5O_2^+$ decomposed to a new H_3O^+. The function is similar to the double-minimum potentials that are often used to describe hydrogen bonds and can provide a handy description of proton transfer dynamics. In addition, to better interpret the proton transfer and the H_2O_2 formation, energetics information of each snapshot has been obtained *via ab initio* DFT. As shown in Fig. 8d, three energy barriers were identified for one successful proton transfer and one HOO hydrogenation event. The energy barrier of forming the first and second H_3O^+ is 0.20 eV and 0.25 eV (Fig. 8d(I–V)), respectively. More importantly, *HOO only needed to overcome a barrier of 0.24 eV to form H_2O_2 by proton transfer.

3.5 H_2O_2 evolution on different g-C_5N_2 surfaces

The aforementioned results have clearly demonstrated that pristine dehydrogenated g-C_5N_2 is effective to catalyze the H_2O/O_2 reaction and produce H_2O_2. The two-step reaction mechanism depends critically on both adsorbed water (at unsaturated C sites) and free water (near the pores of g-C_5N_2). It is important to evaluate the catalytic performance of other models where C and N sites are partially or fully hydrogenated. Similar to Sec. 2.1, 500H_2O and 25 O_2 molecules were randomly placed on both sides of the g-C_5N_2 model, of the size 68.98 Å (y) × 57.71 Å (x). RxMD calculations were performed at 300.0 K for all five models and the results are shown in Fig. 9a. Firstly, g-C_5N_2 showed a general catalytic activity to H_2O/O_2 reactions and H_2O_2 was produced from all five systems. The best yield (eight H_2O_2) was from the pristine g-C_5N_2 (Model 1, no hydrogenation). And two different types of H_2O_2 molecules were synthesized from different hydrogen resources, see Fig. 9c. This phenomenon was also observed in AIMD simulations of Model 3 (Fig. S8 and S9†) and Model 4 (Fig. S10 and S11†). However, only five H_2O_2 molecules were produced in Model 3 where the C-sites are not hydrogenated and the N sites are fully hydrogenated. The

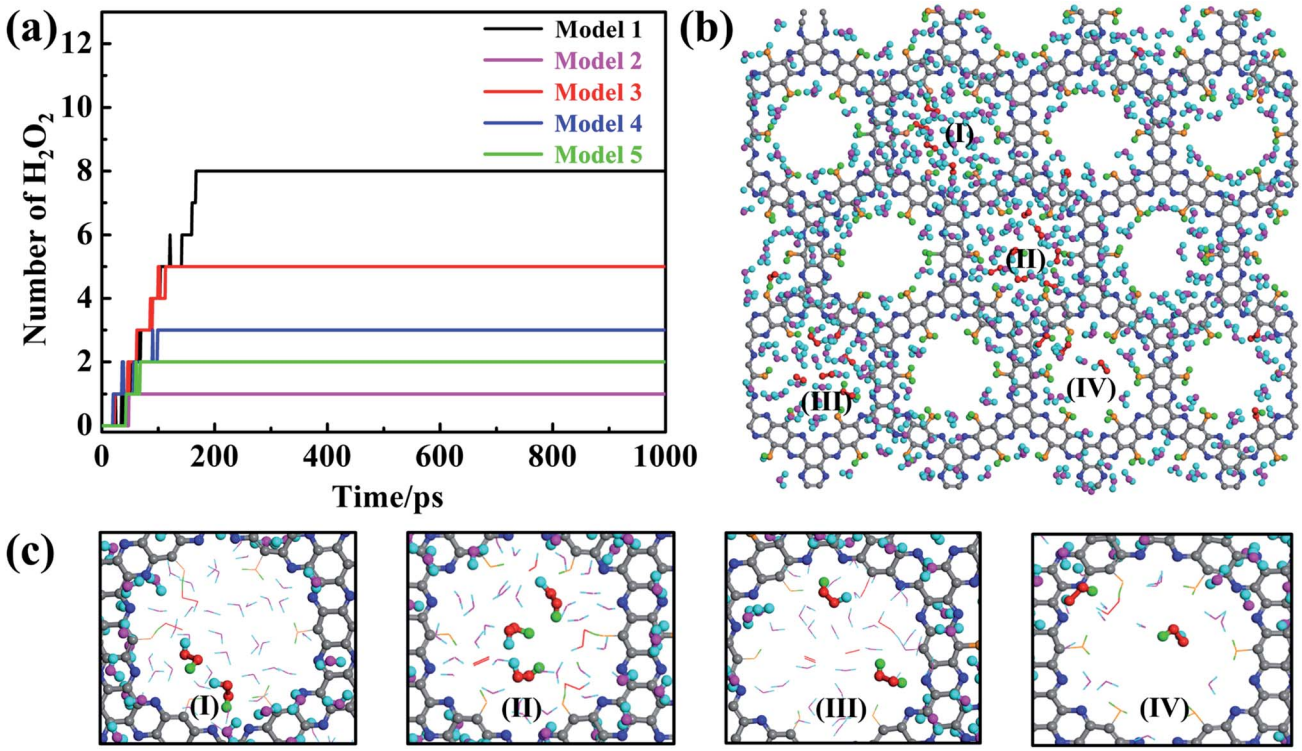

Fig. 9 RxMD simulations of H_2O_2 synthesis on five g-C_5N_2 models at 300.0 K. (a) The number of H_2O_2 molecules produced as a function of simulation time. (b) Snapshots of H_2O and O_2 at the dehydrogenated g-C_5N_2 phase surface described by the RxMD simulations for 200.0 ps. (c) Observed H_2O_2 production from different nanopores of Model 1 as highlighted in (b).

following two observations could explain this result: (a) the transition state calculation indicated that the activation energy of O_2 reaction with H of the edge-N-H species is 0.58 eV (Fig S14(a)†), which is higher than that of O_2 reaction with adsorbed water at the edge C sites. The activation energy for HOO* and H_2O_2 formation was respectively only 0.23 eV and 0.32 eV for Model 1. Thus, O_2 shall preferentially interact with the adsorbed H_2O. (b) As shown in Fig S8,† AIMD calculations reveal that when adsorbed H_2O of edge C sites and hydrogenated H of edge N sites coexist, O_2 preferentially reacted with adsorbed H_2O to form HOO* intermediates. Those HOO* intermediates could then capture H from those edge N sites to form H_2O_2. Based on these observations, we conclude that O_2 reaction with two adsorbed water molecules, as shown for Model 1, is energetically favored and that Model 1 is more active than Mode 3 for the studied H_2O_2 synthesis.

For Model 2 (C-site fully hydrogenated), Model 4 (C-site and N-site fully hydrogenated) and Model 5 (the most stable model, with C sites fully and N sites partially hydrogenated), the yield is relatively lower, only 1, 3 and 2H_2O_2 molecules were produced respectively during the simulation of 1000 ps. According to AIMD results, O_2 can only capture protons from the hydrogenated N sites due to the very stable C–H bonds. In addition, the adsorption configurations of H_2O and O_2 on Model 5 have been optimized *via ab initio* DFT calculations based on Bader charge analysis (Fig. S13a†). The adsorption energy of O_2 is −0.95 eV (Fig. S13b†), and that of H_2O is only −0.05 eV (Fig. S13c†). Stronger O_2 adsorption can significantly weaken the bond energy of O_2, which will reduce the selectivity of H_2O_2 and produce water as a side reaction product. Thus, the number of formed H_2O_2 molecules of Model 4 are more than that of Model 2 and Model 5 with all the edge-C sites hydrogenated.

Although the Gibbs free energy was calculated to evaluate possible g-C_5N_2 hydrogenation, other factors, such as defects and solutions, could also affect the stability and reactivity of g-C_5N_2 catalysts. If one only considers the best reactivity, as shown in Fig. 9a, the pristine g-C_5N_2, in which neither edge nitrogen nor carbon sites are hydrogenated, demonstrates the best catalytic performance, while the most stable g-C_5N_2 model (Model 5) has a relatively poor catalytic performance towards H_2O_2 synthesis. The activity is the major contributor to H_2O_2 synthesis, but the successful application of g-C_5N_2 materials shall also depend strongly on the stability. Regardless of the mechanism or yield of H_2O_2 formation analysis, both suggest that unsaturated edge carbon sites do not promote immediate water dissociation and could be reactivated afterwards. We expect that those unsaturated edge sites are available both from the synthesized g-C_5N_2 and during the process of catalyzing H_2O/O_2 reactions.

4. Conclusion

In summary, this work represents a computational study of direct H_2O_2 synthesis from H_2O and O_2 on a metal-free porous graphitic carbon nitride catalyst. Through a combination of *ab initio* molecular dynamics simulation, reactive molecular

dynamics (RxMD) calculation, and the *ab inito* density functional theory based thermodynamics approach, g-C_5N_2 models with different hydrogenation have been examined to catalyze H_2O/O_2 reactions for H_2O_2 production. The Gibbs free energy calculation and the thermal stability discussion of various g-C_5N_2 models could be a general protocol to screen and evaluate carbon-based materials which are doped with a wide range of other elements. The two-step reaction mechanism has been elucidated, which involves sequentially the adsorption and activation of water at unsaturated C sites of g-C_5N_2, producing HOO* intermediates, and synergetic proton transfer to promote HOO*-to-H_2O_2 reactions, *via* clusters of free and adsorbed water. Other fundamental facts include that pristine g-C_5N_2 is the most active catalyst and that a preferential water adsorption (instead of oxygen adsorption) on g-C_5N_2 is critical to direct H_2O_2 synthesis. Future development of new catalysts could take this as a general criterion to design reactive sites and optimize catalyst geometry, to simultaneously favor water activation at reactive sites and water-chain assisted fast proton transfer processes. This work paves the way for using carbon-based sustainable catalysts for direct H_2O_2 synthesis *via* this promising water/oxygen strategy. In addition, the fundamental insight could also shed light on selecting and designing other green catalysts for heterogeneous oxygen hydrogenation reactions.

Conflicts of interest

The authors declare no competing financial interests.

Acknowledgements

Y. Y. Cao and J. G. Wang acknowledge the support by the National Natural Science Foundation of China (Grant No 21625604, 21671172, 21776251 and 21706229). L.L. Huang acknowledges the U.S. National Science Foundation (NSF) for support through Grant CHE-1710102. We are very pleased to thank the OU Supercomputing Center for Education & Research (OSCER) at the University of Oklahoma for their dedicated support.

References

1 J. M. Campos-Martin, G. Blanco-Brieva and J. L. G. Fierro, *Angew. Chem., Int. Ed.*, 2006, **45**, 6962–6984.
2 E. Brillas, I. Sires and M. A. Oturan, *Chem. Rev.*, 2009, **109**, 6570–6631.
3 N. Agarwal, S. J. Freakley, R. U. McVicker, S. M. Althahban and N. Dimitratos, *Science*, 2017, **358**, 223–227.
4 Y. Yi, L. Wang, G. Li and H. Guo, *Catal. Sci. Technol.*, 2016, **6**, 1593–1610.
5 J. Garcia-Serna, T. Moreno, P. Biasi, M. J. Cocero, J. P. Mikkola and T. O. Salmi, *Green Chem.*, 2014, **16**, 2320–2343.
6 J. K. Edwards, B. Solsona, E. N. Ntainjua, A. F. Carley, A. A. Herzing, C. J. Kiely and G. J. Hutchings, *Science*, 2009, **323**, 1037–1041.
7 Q. Liu, J. C. Bauer, R. E. Schaak and J. H. Lunsford, *Angew. Chem., Int. Ed.*, 2008, **47**, 6221–6224.
8 G. M. Lari, B. Puertolas, M. Shahrokhi, N. Lopez and J. Perez-Ramirez, *Angew. Chem., Int. Ed.*, 2017, **56**, 1775–1779.
9 J. S. Jirkovský, I. Panas, E. Ahlberg, M. Halasa, S. Romani and D. J. Schiffrin, *J. Am. Chem. Soc.*, 2011, **133**, 19432–19441.
10 I. Kim, M.-g. Seo, C. Choi, J. S. Kim, E. Jung, G.-H. Han, J.-C. Lee, S. S. Han, J.-P. Ahn, Y. Jung, K.-Y. Lee and T. Yu, *ACS Appl. Mater. Interfaces*, 2018, **10**, 38109–38116.
11 E. Pizzutilo, S. J. Freakley, S. Cherevko, S. Venkatesan, G. J. Hutchings, C. H. Liebscher, G. Dehm and K. J. J. Mayrhofer, *ACS Catal.*, 2017, **7**, 5699–5705.
12 Y. Shiraishi, Y. Kofuji, H. Sakamoto, S. Tanaka, S. Ichikawa and T. Hirai, *ACS Catal.*, 2015, **5**, 3058–3066.
13 Y. Isaka, Y. Kawase, Y. Kuwahara, K. Mori and H. Yamashita, *Angew. Chem., Int. Ed.*, 2019, **58**, 5402–5406.
14 S. Zhao, T. Guo, X. Li, T. Xu, B. Yang and X. Zhao, *Appl. Catal., B*, 2018, **224**, 725–732.
15 M. Gryszel, A. Markov, M. Vagin and E. D. Głowacki, *J. Mater. Chem. A*, 2018, **6**, 24709–24716.
16 X. Shi, S. Siahrostami, G.-L. Li, Y. Zhang, P. Chakthranont, F. Studt, T. F. Jaramillo, X. Zheng and J. K. Nørskov, *Nat. Commun.*, 2017, **8**, 701.
17 S. Siahrostami, A. Verdaguer-Casadevall, M. Karamad, D. Deiana, P. Malacrida, B. Wickman, M. Escudero-Escribano, E. A. Paoli, R. Frydendal, T. W. Hansen, I. Chorkendorff, I. E. L. Stephens and J. Rossmeisl, *Nat. Mater.*, 2013, **12**, 1137–1143.
18 S. Kato, J. Jung, T. Suenobu and S. Fukuzumi, *Energy Environ. Sci.*, 2013, **6**, 3756.
19 I. Yamanaka and T. Murayama, *Angew. Chem., Int. Ed.*, 2008, **47**, 1900–1902.
20 H. Jing, Q. F. Zhang, N. Large, C. M. Yu, D. A. Blom, P. Nordlander and H. Wang, *Nano Lett.*, 2014, **14**, 3674–3682.
21 C. H. Choi, H. C. Kwon, S. Yook, H. Shin, H. Kim and M. Choi, *J. Phys. Chem. C*, 2014, **118**, 30063–30070.
22 S. Yang, J. Kim, Y. J. Tak, A. Soon and H. Lee, *Angew. Chem., Int. Ed.*, 2016, **55**, 2058–2062.
23 W. R. P. Barros, Q. L. Wei, G. X. Zhang, S. H. Sun, M. R. V. Lanza and A. C. Tavares, *Electrochim. Acta*, 2015, **162**, 263–270.
24 M. B. Zakaria, C. Li, M. Pramanik, Y. Tsujimoto, M. Hu, V. Malgras, S. Tominaka and Y. Yamauchi, *J. Mater. Chem. A*, 2016, **4**, 9266–9274.
25 S. Chen, Z. Chen, S. Siahrostami, D. Higgins, D. Nordlund, D. Sokaras, T. R. Kim, Y. Liu, X. Yan, E. Nilsson, R. Sinclair, J. K. Nørskov, T. F. Jaramillo and Z. Bao, *J. Am. Chem. Soc.*, 2018, **140**, 7851–7859.
26 T.-P. Fellinger, F. Hasché, P. Strasser and M. Antonietti, *J. Am. Chem. Soc.*, 2012, **134**, 4072–4075.
27 L. Han, Y. Sun, S. Li, C. Cheng, C. E. Halbig, P. Feicht, J. L. Hübner, P. Strasser and S. Eigler, *ACS Catal.*, 2019, **9**, 1283–1288.
28 J. Park, Y. Nabae, T. Hayakawa and M. a. Kakimoto, *ACS Catal.*, 2014, **4**, 3749–3754.

29 Y. Cao, S. Deng, Q. Fang, X. Sun, C. Zhao, J. Zheng, Y. Gao, H. Zhuo, Y. Li, Z. Yao, Z. Wei, X. Zhong, G. Zhuang and J. Wang, *Nanotechnology*, 2019, **30**, 335403.
30 K. Gong, F. Du, Z. Xia, M. Durstock and L. Dai, *Science*, 2009, **323**, 760–764.
31 Z. Pan, K. Wang, Y. Wang, P. Tsiakaras and S. Song, *Appl. Catal., B*, 2018, **237**, 392–400.
32 L. Tao, Q. Wang, S. Dou, Z. Ma, J. Huo, S. Wang and L. Dai, *Chem. Commun.*, 2016, **52**, 2764–2767.
33 P. Zhang, D. Sun, A. Cho, S. Weon, S. Lee, J. Lee, J. W. Han, D.-P. Kim and W. Choi, *Nat. Commun.*, 2019, **10**, 940.
34 Z. Lu, G. Chen, S. Siahrostami, Z. Chen, K. Liu, J. Xie, L. Liao, T. Wu, D. Lin, Y. Liu, T. F. Jaramillo, J. K. Norskov and Y. Cui, *Nat. Catal.*, 2018, **1**, 156–162.
35 H. W. Kim, M. B. Ross, N. Kornienko, L. Zhang, J. Guo, P. Yang and B. D. McCloskey, *Nat. Catal.*, 2018, **1**, 282–290.
36 V. Briega-Martos, A. Ferre-Vilaplana, A. de la Peña, J. L. Segura, F. Zamora, J. M. Feliu and E. Herrero, *ACS Catal.*, 2016, **7**, 1015–1024.
37 Y. Kou, Y. Xu, Z. Guo and D. Jiang, *Angew. Chem., Int. Ed.*, 2011, **50**, 8753–8757.
38 Z.-D. Yang, W. Wu and X. C. Zeng, *J. Mater. Chem. C*, 2014, **2**, 2902–2907.
39 A. C. T. van Duin, S. Dasgupta, F. Lorant and W. A. Goddard, *J. Phys. Chem. A*, 2001, **105**, 9396–9409.
40 K. Chenoweth, A. C. T. van Duin and W. A. Goddard III, *J. Phys. Chem. A*, 2008, **112**, 1040–1053.
41 L. L. Huang, M. Seredych, T. J. Bandosz, A. C. T. van Duin, X. H. Lu and K. E. Gubbins, *J. Chem. Phys.*, 2013, **139**, 194707.
42 S. Plimpton, *J. Comput. Phys.*, 1995, **117**, 1–19.
43 S. Nose, *J. Chem. Phys.*, 1984, **81**, 511–519.
44 W. G. Hoover, *Phys. Rev. A*, 1985, **31**, 1695–1697.
45 L. Verlet, *Phys. Rev.*, 1967, **159**, 98–103.
46 P. E. Blochl, *Phys. Rev. B: Condens. Matter Mater. Phys.*, 1994, **50**, 17953–17979.
47 G. Kresse and J. Furthmuller, *Comput. Mater. Sci.*, 1996, **6**, 15–50.
48 G. Kresse and D. Joubert, *Phys. Rev. B: Condens. Matter Mater. Phys.*, 1999, **59**, 1758–1775.
49 J. P. Perdew, K. Burke and M. Ernzerhof, *Phys. Rev. Lett.*, 1996, **77**, 3865–3868.
50 S. Grimme, J. Antony, S. Ehrlich and H. Krieg, *J. Chem. Phys.*, 2010, **132**, 154104.
51 R. A. Evarestov and V. P. Smirnov, *Phys. Rev. B: Condens. Matter Mater. Phys.*, 2004, **70**, 233101.
52 G. Henkelman, B. P. Uberuaga and H. Jonsson, *J. Chem. Phys.*, 2000, **113**, 9901–9904.
53 J. VandeVondele, M. Krack, F. Mohamed, M. Parrinello, T. Chassaing and J. Hutter, *Comput. Phys. Commun.*, 2005, **167**, 103–128.
54 W. G. Hoover, *Phys. Rev. A*, 1985, **31**, 1695–1697.
55 J. VandeVondele and J. Hutter, *J. Chem. Phys.*, 2007, **127**, 114105.
56 G. Lippert, J. Hutter and M. Parrinello, *Mol. Phys.*, 1997, **92**, 477–487.
57 F. Bottin, F. Finocchi and C. Noguera, *Phys. Rev. B: Condens. Matter Mater. Phys.*, 2003, **68**, 13.
58 E. Heifets, S. Piskunov, E. A. Kotomin, Y. F. Zhukovskii and D. E. Ellis, *Phys. Rev. B: Condens. Matter Mater. Phys.*, 2007, **75**, 13.
59 Q. Cai, J.-g. Wang, Y. Wang and D. Mei, *J. Phys. Chem. C*, 2016, **120**, 19087–19096.
60 D. Gao, H. Zhou, F. Cai, D. Wang, Y. Hu, B. Jiang, W.-B. Cai, X. Chen, R. Si, F. Yang, S. Miao, J. Wang, G. Wang and X. Bao, *Nano Res.*, 2017, **10**, 2181–2191.
61 K. Reuter and M. Scheffler, *Phys. Rev. B: Condens. Matter Mater. Phys.*, 2003, **68**, 045407.
62 https://webbook.nist.gov/.
63 R. Cao, J.-S. Lee, M. Liu and J. Cho, *Adv. Energy Mater.*, 2012, **2**, 816–829.
64 Z. L. Wang, D. Xu, J. J. Xu and X. B. Zhang, *Chem. Soc. Rev.*, 2014, **43**, 7746–7786.
65 R. Ma, G. Lin, Y. Zhou, Q. Liu, T. Zhang, G. Shan, M. Yang and J. Wang, *npj Comput. Mater.*, 2019, **5**, 78.
66 L. Yu, X. Pan, X. Cao, P. Hu and X. Bao, *J. Catal.*, 2011, **282**, 183–190.
67 J. Goclon and K. Winkler, *Appl. Surf. Sci.*, 2018, **462**, 134–141.
68 O. Gerlits, T. Wymore, A. Das, C. H. Shen, J. M. Parks, J. C. Smith, K. L. Weiss, D. A. Keen, M. P. Blakeley, J. M. Louis, P. Langan, I. T. Weber and A. Kovalevsky, *Angew. Chem., Int. Ed.*, 2016, **55**, 4924–4927.
69 C. T. Supuran, *Biochem. J.*, 2016, **473**, 2023–2032.
70 E. Nango, A. Royant, M. Kubo, T. Nakane, C. Wickstrand, T. Kimura, T. Tanaka, K. Tono, C. Y. Song, R. Tanaka, T. Arima, A. Yamashita, J. Kobayashi, T. Hosaka, E. Mizohata, P. Nogly, M. Sugahara, D. Nam, T. Nomura, T. Shimamura, D. Im, T. Fujiwara, Y. Yamanaka, B. Jeon, T. Nishizawa, K. Oda, M. Fukuda, R. Andersson, P. Bath, R. Dods, J. Davidsson, S. Matsuoka, S. Kawatake, M. Murata, O. Nureki, S. Owada, T. Kameshima, T. Hatsui, Y. Joti, G. Schertler, M. Yabashi, A. N. Bondar, J. Standfuss, R. Neutze and S. Iwata, *Science*, 2016, **354**, 1552–1557.
71 C. Chen, T. Shi, W. Chang and J. Zhao, *ChemCatChem*, 2015, **7**, 724–731.
72 K. Yamamoto and K. Takatsuka, *Phys. Chem. Chem. Phys.*, 2018, **20**, 6708–6725.
73 A. Badalyan and S. S. Stahl, *Nature*, 2016, **535**, 406–410.
74 C. W. Lee, J. S. Hong, K. D. Yang, K. Jin, J. H. Lee, H.-Y. Ahn, H. Seo, N.-E. Sung and K. T. Nam, *ACS Catal.*, 2018, **8**, 931–937.
75 Q. Ly, B. V. Merinov, H. Xiao, W. A. Goddard and T. H. Yu, *J. Phys. Chem. C*, 2017, **121**, 24408–24417.
76 M. T. M. Koper, *Chem. Sci.*, 2013, **4**, 2710–2723.
77 U. W. Schmitt and G. A. Voth, *J. Chem. Phys.*, 1999, **111**, 9361–9381.
78 S. Hammes-Schiffer, *Acc. Chem. Res.*, 2001, **34**, 273–281.
79 J. M. Saveant, *Acc. Chem. Res.*, 1993, **26**, 455–461.
80 S. Scheiner, *Acc. Chem. Res.*, 1985, **18**, 174–180.
81 M. H. V. Huynh and T. J. Meyer, *Chem. Rev.*, 2007, **107**, 5004–5064.
82 D. R. Weinberg, C. J. Gagliardi, J. F. Hull, C. F. Murphy, C. A. Kent, B. C. Westlake, A. Paul, D. H. Ess, D. G. McCafferty and T. J. Meyer, *Chem. Rev.*, 2012, **112**, 4016–4093.

83 R. I. Cukier and D. G. Nocera, *Annu. Rev. Phys. Chem.*, 1998, **49**, 337–369.
84 J. M. Mayer, *Annu. Rev. Phys. Chem.*, 2004, **55**, 363–390.
85 S. Hammes-Schiffer and A. A. Stuchebrukhov, *Chem. Rev.*, 2010, **110**, 6939–6960.
86 M. Eigen, *Angew. Chem.*, 1963, **75**, 489–508.
87 M. Eigen, *Angew. Chem., Int. Ed.*, 1964, **3**, 1–72.
88 G. Zundel, *Adv. Chem. Phys.*, 2000, **111**, 1–217.
89 D. Marx, *ChemPhysChem*, 2006, **7**, 1848–1870.